catalysts

MDPI

Article

Composite CdS/TiO_2 Powders for the Selective Reduction of 4-Nitrobenzaldehyde by Visible Light: Relation between Preparation, Morphology and Photocatalytic Activity

Martina Milani [1], Michele Mazzanti [1], Stefano Caramori [1], Graziano Di Carmine [1], Giuliana Magnacca [2] and Alessandra Molinari [1,*]

[1] Dipartimento di Scienze Chimiche, Farmaceutiche ed Agrarie, Università di Ferrara, Via L. Borsari 46, 44121 Ferrara, Italy
[2] Dipartimento di Chimica, Università di Torino, Via P. Giuria 7, 10125 Torino, Italy
* Correspondence: alessandra.molinari@unife.it; Tel.: +39-0532-455378

Abstract: A series of composite CdS/TiO_2 powders was obtained by nucleation of TiO_2 on CdS nanoseeds. This combination presents the appropriate band edge position for photocatalytic redox reactions: visible light irradiation of CdS allows the injection of electrons into dark TiO_2, increasing the lifetimes of separated charges. The electrons have been used for the quantitative photoreduction of 4-nitrobenzaldehyde to 4-aminobenzaldehyde, whose formation was pointed out by ^{1}H NMR and ESI-MS positive ion mode. Concomitant sacrificial oxidation of 2-propanol, which was also the proton source, occurred. The use of characterization techniques (XRD, N_2 adsorption-desorption) evidenced the principal factors driving the photocatalytic reaction: the nanometric size of anatase crystalline domains, the presence of dispersed CdS to form an extended active junction CdS/anatase, and the presence of mesopores as nanoreactors. The result is an efficient photocatalytic system that uses visible light. In addition, the presence of TiO_2 in combination with CdS improves the stability of the photoactive material, enabling its recyclability.

Keywords: cadmium sulfide; titanium dioxide; visible light; photocatalysis; nitroaromatic photoreduction; composite powders

Citation: Milani, M.; Mazzanti, M.; Caramori, S.; Di Carmine, G.; Magnacca, G.; Molinari, A. Composite CdS/TiO_2 Powders for the Selective Reduction of 4-Nitrobenzaldehyde by Visible Light: Relation between Preparation, Morphology and Photocatalytic Activity. *Catalysts* **2023**, *13*, 74. https://doi.org/10.3390/catal13010074

Academic Editors: Orhan Şişman, Surjyakanta Rana, José Joaquín Velázquez García and Rajesh Dagupati

Received: 21 November 2022
Revised: 22 December 2022
Accepted: 27 December 2022
Published: 30 December 2022

1. Introduction

Photocatalysis is receiving ever-growing interest since it provides a greener alternative to the conventional synthetic processes. In fact, mild conditions, short reaction sequences and the decrease of production of undesired by-products highlight its potential as an efficient method for organic transformation [1].

TiO_2 is the traditional semiconductor material which has been employed since the 1970s in the field of degradation of pollutants, DSSC, gas sensors, batteries etc., due to its chemical stability, low cost, and low toxicity [2,3]. However, its wide band gap (about 3.2 eV) limits the use of visible light contained in the solar spectrum at higher frequencies, and despite the charge mobility of TiO_2, rapid recombination of photogenerated charge carriers occurs. To overcome the barriers, combining TiO_2 with a narrow band gap semiconductor is of considerable interest.

Fe_2O_3 [4], Cu_2O [5] and WO_3 [6] have been used, but cadmium sulfide (CdS) is one of the best, both because of its band gap value (2.4 eV) and appropriate band edge position for photocatalytic redox reactions [7]. Spectral response of CdS/TiO_2 systems can be extended to the visible light region and the appropriate matching of band edges allows the injection of electrons generated from CdS into TiO_2, effectively increasing the lifetimes of separated charges [7–22]. Moreover, some negative aspects typical of CdS itself, such as easy agglomeration and poor photostability, can be improved in the combined photocatalyst. For these reasons, CdS/TiO_2 composite systems attract intensive studies and have been employed in oxidation

and reduction processes. Most of them refer to crystalline or nanostructured materials and have been investigated in the photoelectrocatalytic cells for hydrogen evolution [7,16,23,24], in the photocatalytic degradation of organic pollutants [19,20,25] and dyes [9,11–15,24], and in some reductive transformations [13,14,26]. When UV-vis illumination is employed, an improvement of photoactivity, with respect to TiO_2 alone, is usually observed due to the presence of CdS [21,22]. However, the favourable effect of the heterojunction among TiO_2 and CdS is observed only when CdS is illuminated with visible light ($\lambda > 420$ nm) [26].

Considering organic transformations, the selective reduction of aromatic nitro compounds to amines is one of the most fundamental reactions in organic synthesis, because the corresponding anilines are widely utilized in the dyes, agricultural and pharmaceutical industries [13,27]. Since amines can be obtained by catalytic hydrogenation of aromatic nitro compounds under harsh reaction conditions and selective reduction of the nitro group in the presence of other reducible functional groups such as carbonyl, halide and cyano, it is difficult to achieve the development of a simple, low impact and highly efficient method for the selective reduction of the nitro group. We and many other researchers demonstrated that photoexcited TiO_2 [28–33], doped TiO_2 [34] or composite photocatalysts based on TiO_2 [35–37] were able to catalyze the reduction of nitroaromatic compounds to the corresponding anilines. In addition, when two reducible functionalities are simultaneously present in the molecules (e.g., *p*-nitrobenzaldehyde), the selectivity of the reaction could be controlled by the presence of small alkali metal ions such as Li^+ and Na^+ [38].

In this work, we explore a series of new composite materials based on CdS/TiO_2 prepared by hydrolysis of a titania precursor in a colloidal solution of CdS nanoparticles (CdS/TiO_2-(1–4)). Exploiting the appropriate band edge position of TiO_2 and CdS, we focus on the selective visible illumination of CdS and on the subsequent injection of electrons in the conduction band of dark TiO_2. In principle, all the reductive transformations carried out by UV illumination of TiO_2 should be feasible by visible irradiation of CdS in CdS/TiO_2. The target reaction chosen here is the selective reduction of *p*-nitrobenzaldehyde to the corresponding aniline. Textural and spectral properties of the prepared materials will be related to their photocatalytic performances. To our knowledge, the research reported here is a rare example of a selective and efficient photocatalytic transformation occurring under mild conditions using visible light with a CdS-based photocatalyst with good stability.

2. Results and Discussion

2.1. Materials Characterization

The morphological characterization of CdS/TiO_2-(1–4) samples is discussed in this section. Table 1 presents the obtained information together with details from the preparation procedure.

Table 1. Morphological features and preparation details of CdS/TiO_2-(1–4) materials.

	CdS/TiO_2-1	**CdS/TiO_2-2**	**CdS/TiO_2-3**	**CdS/TiO_2-4**
CdS/Ti(OiPr)$_4$ molar ratio in initial solution	1/16	1/16	1/16	1/8
Aging time at 90 °C (h)	0	1	3	1
SSA ($m^2\ g^{-1}$)	446 ± 22	205 ± 10	210 ± 10	210 ± 10
V_{tot} ($cm^3\ g^{-1}$)	0.45	0.23	0.28	0.13
$V_{meso/macro}$ (>17 Å width, $cm^3\ g^{-1}$)	0.39	0.20	0.25	0.08
V_{micro} (<17 Å width, $cm^3\ g^{-1}$)	0.06	0.03	0.03	0.05

2.1.1. Structural and Textural Properties of CdS/TiO_2-(1–4)

The XRD patterns of CdS/TiO_2-(1–4) samples, compared with the diffractogram of parent TiO_2, are reported in Figure 1.

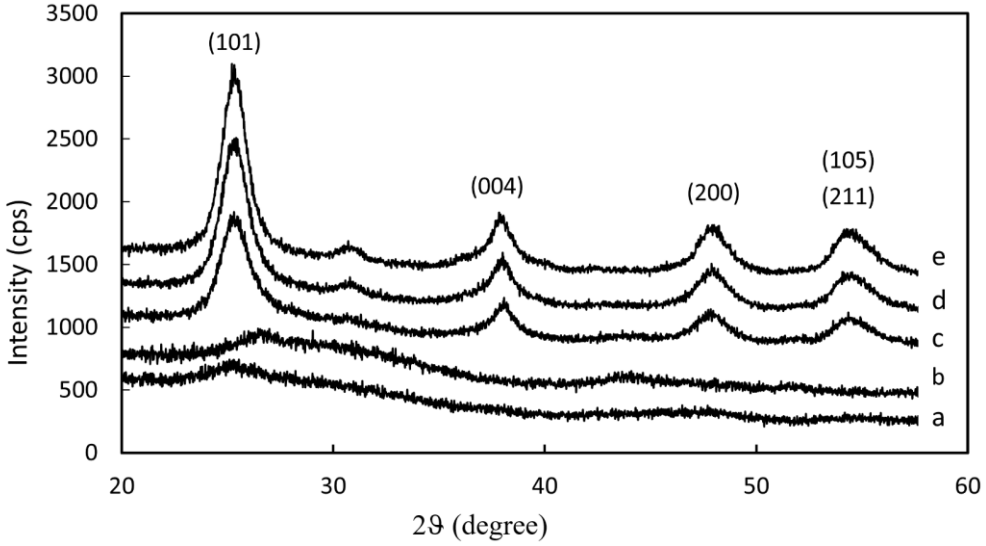

Figure 1. XRD patterns of TiO_2 (**a**), CdS/TiO_2-1 (**b**), CdS/TiO_2-4 (**c**), CdS/TiO_2-2 (**d**) and CdS/TiO_2-3 (**e**).

CdS/TiO_2-1 shows the typical profile of an amorphous material, presenting only some wide halos related to the presence of the short range order anatase phase of TiO_2 (at $2\theta \approx 25°$, JCPDS pattern 00-021-1272) [39] and probably some residues of very small crystalline arrays of hawleyite phase of cubic CdS (at $2\theta \approx 31°$, coupled to the weak halo at 45°, JCPDS card 00-010-0454), as the positions correspond to the two principal reflections of that phase. It is not possible to exclude that the signal at 31° is related to the presence of short-range order brookite (at $2\theta \approx 31°$, JCPDS pattern 00-076-1934), as reported by other authors [40].

The aging carried out at 90 °C causes an increase of crystallinity, all the samples and the main reflections of anatase phase are now clearly visible in the diffractograms. In agreement with the Debye–Scherrer equation, the crystalline domains of CdS/TiO_2-2 and CdS/TiO_2-3, slightly increase with aging time and never exceed the size of 10 nm, whereas an increase of CdS/TiO_2 ratio in CdS/TiO_2-4 generates smaller crystals of anatase whose size is lower than 5 nm. The aging process also affects the signal at 31°, which is much more easily detectable in the diffractogram, albeit remaining very weak in intensity. If the 31° peak is assigned to the CdS phase, it seems to be possible to confirm the hypothesis reported in Ref. [40] that CdS colloidal particles behave as seeds for the TiO_2 crystallization process for two main reasons: (a) the TiO_2 crystals growing at the surface of CdS nanoparticles in all the aged samples CdS/TiO_2 hamper the coalescence and consequent crystallization of CdS nanoparticles, which remain in a very well dispersed state after the aging process; (b) an increase of CdS/TiO_2 ratio, as in the sample CdS/TiO_2-4, avoids an extended growth of titania crystals after nucleation on CdS.

To better investigate the nanometric structure of the materials, HRTEM was applied to the analysis of the most representative samples, namely CdS/TiO_2-1 and CdS/TiO_2-2, and the resulting images are reported in Figure 2.

The appearance of the diffractograms is reported in Figure 1, both samples are microcrystalline, however, some differences can be observed. First of all, the images at low magnification allow one to observe the aggregation state of the particles: sample CdS/TiO_2-1 presents a more compact arrangement than CdS/TiO_2-2, as expected considering an aggregation occurring among smaller particles. Secondly, the images at high magnification allow one to observe the presence and extension of the fringe patterns, i.e., the presence and extension of the crystalline domains: they are more limited in size and less visible in the case of CdS/TiO_2-1.

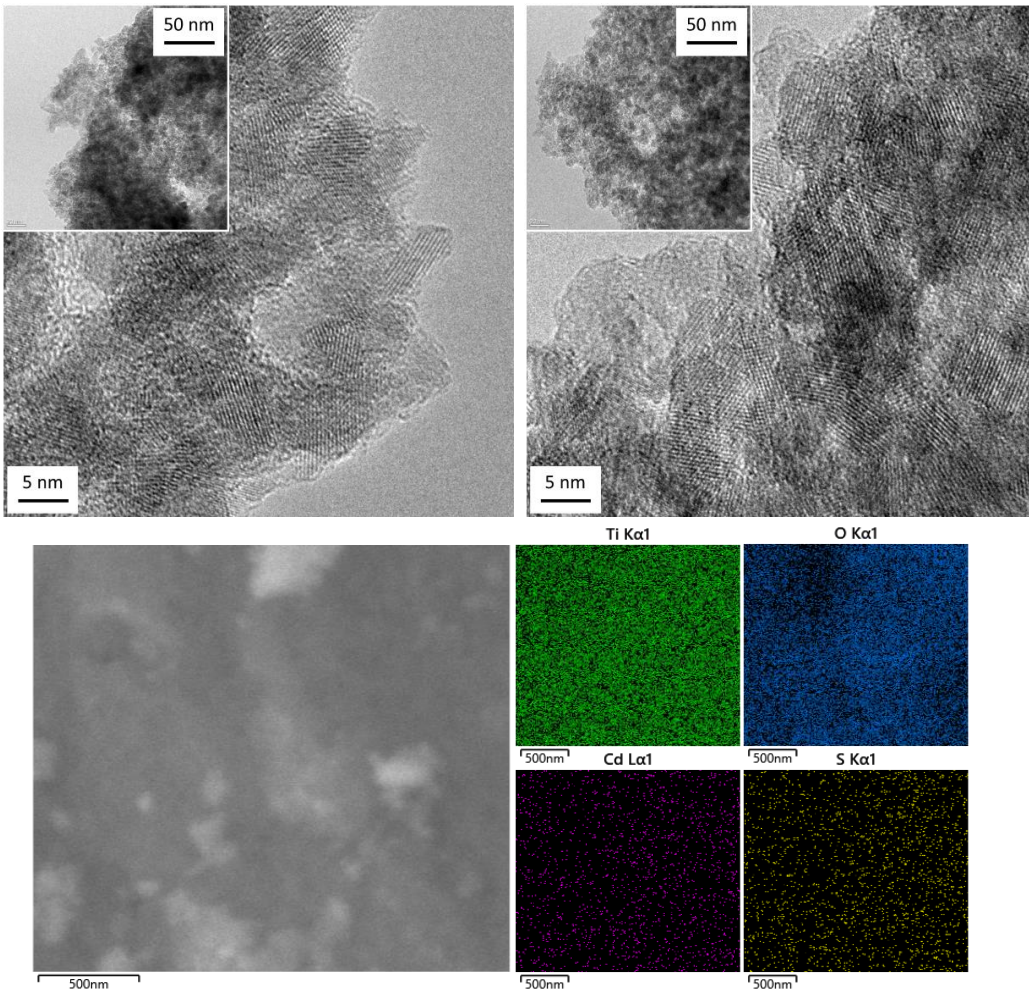

Figure 2. Upper section: HRTEM images of CdS/TiO_2-1 (**left**) and CdS/TiO_2-2 (**right**) at low and high magnification. Lower section: FESEM secondary electron images and corresponding Ti, O, Cd and S EDS maps.

Unfortunately, the analysis of the diffraction patterns does not allow one to identify the two expected crystalline phases, TiO_2 anatase and CdS hawleyite, as most parts of the fringes observed correspond to d_{hkl} values in the range 3.44−3.64 Å, which could be more easily correlated to anatase crystals without excluding the presence of hawleyite crystals. For a further confirmation, EDS maps related to the presence of Ti, O, Cd and S elements in a portion of the sample CdS/TiO_2-1 are reported in the bottom section of Figure 2. All the expected components are visible in the image and are similarly dispersed in the whole region, without any possibility to evidence portions made of TiO_2 and/or CdS, neither to study the junctions between the two compounds.

Gas-volumetric adsorption of N_2 at low temperature gives important information about the specific surface area and the pore size distribution of the CdS/TiO_2 systems (Figure S1). Specific surface area and pore volume data of all the investigated materials are summarized in Table 1. Amorphous CdS/TiO_2-1 has an SSA of 446 m^2/g, lower with respect to that of TiO_2 prepared under the same experimental conditions (505 m^2/g, not reported in the manuscript for the sake of brevity), indicating a growth of the particles' size after the TiO_2 synthesis. A decrease of area (about 45–55%) [41] and porosity is observed after aging, with the most important effect evidenced by the sample CdS/TiO_2-4, which seems to become denser (i.e., with less mesopores) than the others during the treatment (Figure S1). This aspect could affect the activity of the catalyst if the mesoporosity plays a non-negligible role behaving as an active surface available to reactants.

The porosity of the systems examined in the curves of pore size and pore area distribution in Figure S1, can be produced by the aggregation of the primary particles creating void interparticle spaces, as the TEM images allow excluding the presence of intraparticle porosity. In this view, a change of porosity can be related to a modification of the particles' aggregation that could be caused by two main phenomena. (a) The heating phase at 90 °C produces some sintering of the particles that become bigger. The effect increases with the treatment duration. In this case, it should be possible to observe a decrease of material specific surface area. (b) The presence of a higher ratio CdS/TiO_2 produces smaller TiO_2 particles that can aggregate in a more compact network decreasing the porosity of the material. This change not necessarily affects the specific surface area value. To check which one of the two phenomena is playing a role in the studied systems, we can observe the values of area and porosity of CdS/TiO_2-2 and CdS/TiO_2-3. The latter sample has been treated at 90 °C for 3 h and the sintering effect, if present, should be more evident than for the first material treated for a shorter time. No significant changes of the textural features of the two samples were evidenced, therefore one can conclude the sintering effect is negligible in these conditions. On the other hand, an increase of the ratio CdS/TiO_2, keeping constant the duration of the thermal treatment at 90 °C, as in the samples CdS/TiO_2-4 compared with CdS/TiO_2-2, has a visible effect on the porosity observed and this suggests that the modification of porosity is mainly due to the extensive aggregation created among smaller TiO_2 particles.

2.1.2. Single Photon Time Emission Decays of CdS/TiO_2-1 and CdS/TiO_2-2

Time resolved analysis of the fluorescence of CdS/TiO_2-1 and CdS/TiO_2-2 is reported in Figures S2 and S3, respectively. The decay of CdS/TiO_2-1 was satisfactorily fitted with a bi-exponential function, where the dominant component (>95%) is below the instrumental resolution of the apparatus (<300 ps), while the smaller amplitude (~5%) was longer lived (2.36 ns). When observing CdS/TiO_2-2 (Figure S3), a tri-exponential function acceptably fits the decay, consistent with a distribution of sites from which the radiative recombination of charges occurs with different rate constants. As before, the dominant component (~90%) is very fast, while a smaller amplitude (~1%) was much longer lived and decayed in the nanosecond time scale (8.4 ns). Pure CdS emission decay was very fast and below the instrumental resolution. Interestingly, the ns radiative recombination of the carriers was faster on CdS/TiO_2-1 than on CdS/TiO_2-2, indicating that in the more crystalline material, with a better developed band structure, the charge separation could be better achieved and maintained for longer times. The long-lived emission tail in CdS-TiO_2-2 is consistent with the radiative recombination of electrons injected and trapped into TiO_2 with the hole residing in CdS, occurring at the interface between the two materials. This is facilitated by the high and homogeneous dispersion of CdS in TiO_2 (Figure 2).

2.1.3. Spectral Properties of CdS/TiO_2-(1–4)

UV-visible DR spectra of CdS/TiO_2-(1–4) samples are reported in Figure 3. We observe an increase of light-harvesting efficiency from wavelengths of 400 nm and above, where CdS manifests its maximum absorption [42].

Estimation of the band gap values of the two semiconductors has been carried out using the baseline method, as proposed by Macyk [43] for multicomponent systems and not by the direct application of the Tauc method (Figure S4). In Table S1 the estimated band gap values: 3.3 eV for TiO_2 and 2.1–2.2 eV for CdS are reported.

Considering the optical properties of the materials, it is evident that in the CdS/TiO_2-(1–4) samples, the sulfide is the only photoactive component when visible light ($\lambda > 420$ nm) is employed.

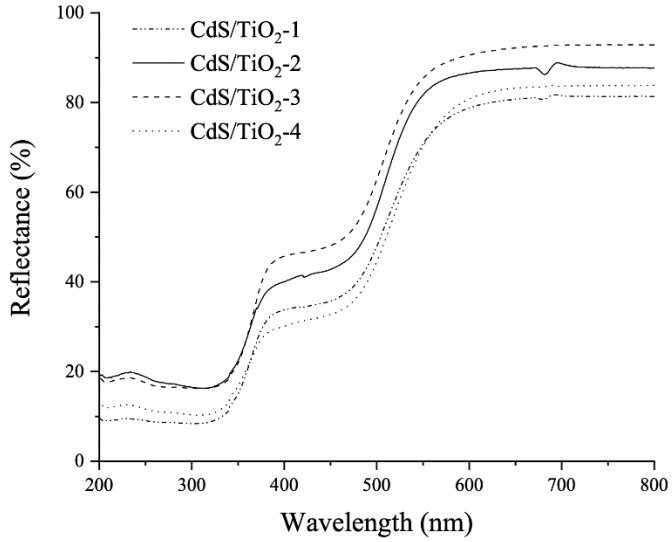

Figure 3. UV-vis DR spectra of CdS/TiO_2-(1–4) materials.

2.2. Photocatalytic Properties of CdS/TiO$_2$-(1–4)

With the aim of exploiting the appropriate band edge position of the two semiconductors, we focussed on the visible illumination ($\lambda \geq 420$ nm) of CdS and the subsequent injection of electrons in the conduction band of dark TiO_2 for the selective reduction of *p*-nitrobenzaldehyde (NBA) to the corresponding 4-amino benzaldehyde (ABA).

First, we gained information about the interaction of NBA with the surface of the photocatalytic material. Figure 4 shows the IR spectra of NBA adsorbed on CdS/TiO_2 both kept in the dark and irradiated in the visible region ($\lambda \geq 420$ nm). In the infrared spectrum of NBA adsorbed on the material before irradiation (dashed line), two absorption bands at 1541 cm^{-1} and 1346 cm^{-1} which are attributable to the asymmetric and symmetric N-O stretching frequencies of the nitro group are recognizable [28,29,33]. This indicates that the nitroaromatic molecule interacted with the TiO_2 surface mainly through this functional group, in agreement to what has been previously observed [29]. Therefore, visible irradiation should involve the nitro group and, accordingly, the stretching values assigned to the N-O vibrations almost completely disappear in the IR spectrum after the irradiation period (solid line). This result suggests a strong interaction between the functional group and the surface.

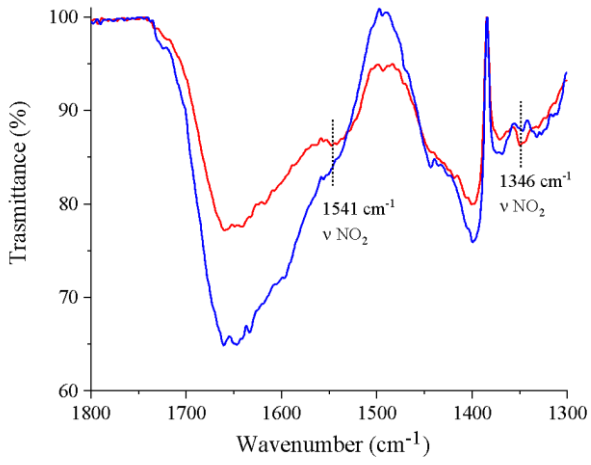

Figure 4. Infrared spectra of 4-nitrobenzaldehyde adsorbed on CdS/TiO_2 before (**red**) and after 150′ visible irradiation (**blue**).

With these preliminary results in hand, an optimum amount (3 g/L) of each CdS/TiO_2-(1–4) powder was suspended in a CH_3CN/2-PrOH (4/1, 3 mL) solution containing NBA (1×10^{-4} M) and degassed (20′) by N_2 bubbling. Therefore, the suspension was visibly irradiated ($\lambda \geq 420$ nm), keeping the best stirring conditions. At prefixed time intervals, the irradiation was stopped, and the mixture was centrifuged, filtered and UV-visible spectra were recorded. Figure 5 reports the main spectral variations obtained with CdS/TiO_2-2. It is observed that the absorption maximum of starting NBA (λ_{max} = 264 nm) decreased during time while that of ABA (λ_{max} = 312 nm) increased. From the absorbance values, we obtained the concentration profiles of NBA and ABA.

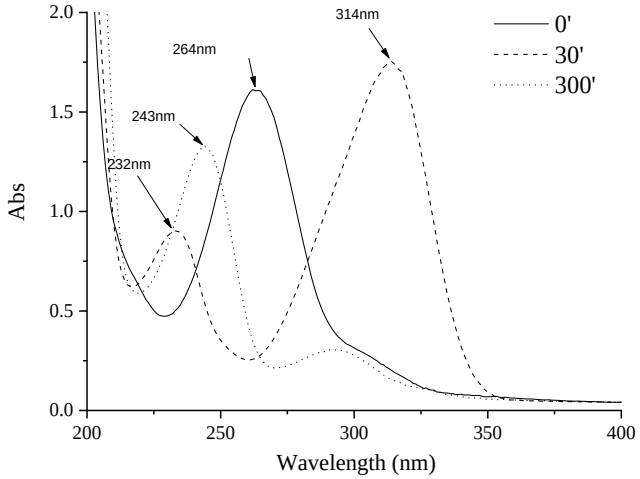

Figure 5. Spectral changes obtained upon visible irradiation (30 and 300 min) of a deaerated suspension of CdS/TiO_2-2 (3 g/L) in CH_3CN/2-PrOH (4/1, 3 mL) mixture containing NBA (1×10^{-4} M).

Figure 6 reports data obtained with the most performant CdS/TiO_2-2. It was observed that after 30 min of irradiation the conversion of NBA was higher than 95%. The mass balance was almost complete.

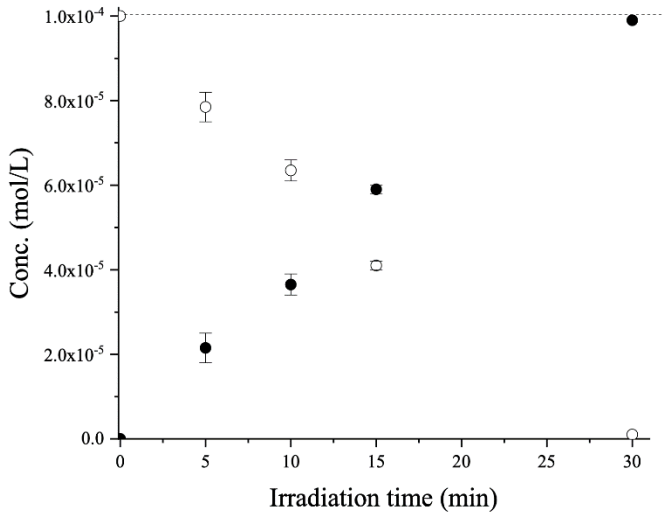

Figure 6. Time courses of NBA (1×10^{-4} M, empty circles) and of ABA (full circles) during irradiation ($\lambda \geq 420$ nm, 25 °C) of CdS/TiO_2-2 (3 g/L) suspended in a deaerated CH_3CN/2-PrOH (4/1) reaction mixture. The horizontal dotted line represents the initial amount of NBA in the reaction container and allows evidencing the almost complete transformation of NBA in ABA product (yield > 95%).

The formation of 4-amino benzaldehyde (ABA) is evidenced in both the ^{1}H-NMR and ESI-MS spectrum of the irradiated solution (Figure 7). By comparing the ^{1}H-NMR spectrum of reaction (after 30 min of irradiation) with the spectra of 4-nitrobenzaldehyde

and 4-aminobenzaldehyde, the consumption of the starting material in concomitance with the formation of target product is clearly evident. In particular, the disappearance of the diagnostic peak of aldehyde of 4-nitrobenzaldehyde at 10.16 ppm and the appearance of the new peak at 9.76 ppm, which is attributable to 4-aminobenzaldehyde, undoubtably shows the selective reduction of the nitro group. Furthermore, this is corroborated by the ESI-MS spectrum, which presents the M + 1 peak at 122.03 m/z relative to protonated aminobenzaldehyde:

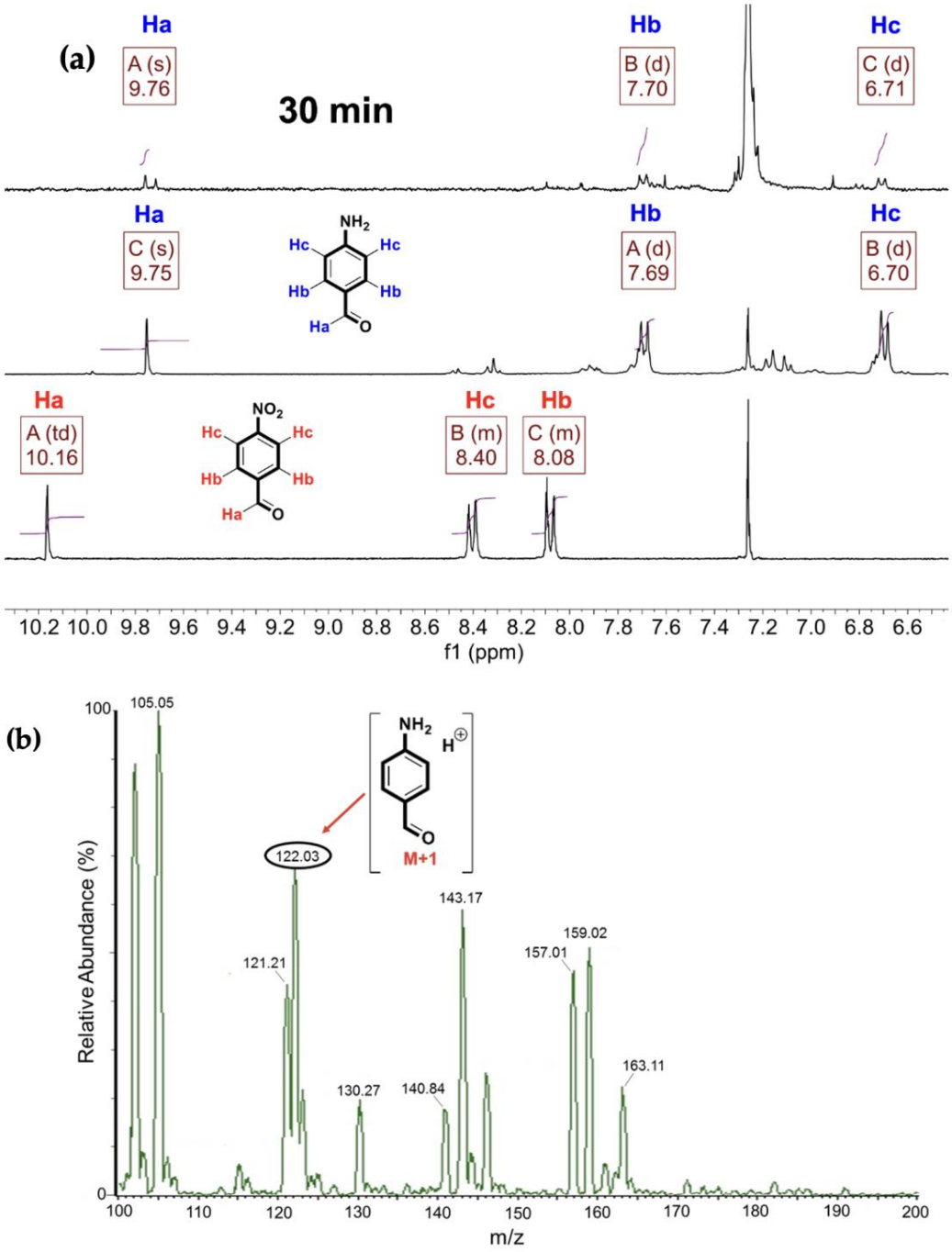

Figure 7. (**a**) from bottom to top the spectra of 4-nitrobenzaldehyde (NBA), 4-aminobenzaldehyde (ABA) and crude of reaction after 30 min of irradiation; (**b**) on right the ESI-MS spectrum of crude of reaction after 30 min.

Control experiments showed that the suspension kept in the dark and the visible (λ > 420 nm) irradiation of the solution containing NBA in the absence of the photocatalyst or in the presence of sole TiO_2 did not lead to any reaction. Moreover, CdS/TiO_2-2 is more efficient than commercial CdS (Figure S6), indicating that the presence of TiO_2 leads to an increase of separated charges lifetime, in agreement with fast techniques and the HRTEM results discussed earlier. This evidence confirms that a visible irradiation (30 min) of CdS/TiO_2-2 is enough to obtain a full conversion of the nitro group into the aminic one. As reported before by some of us in the case of TiO_2 P-25 [28], protons generated during 2-PrOH oxidation on the photogenerated holes are consumed in the reduction of NBA to ABA (Equations (1)–(3)) and a schematization of the overall photocatalytic mechanism is proposed in Scheme 1:

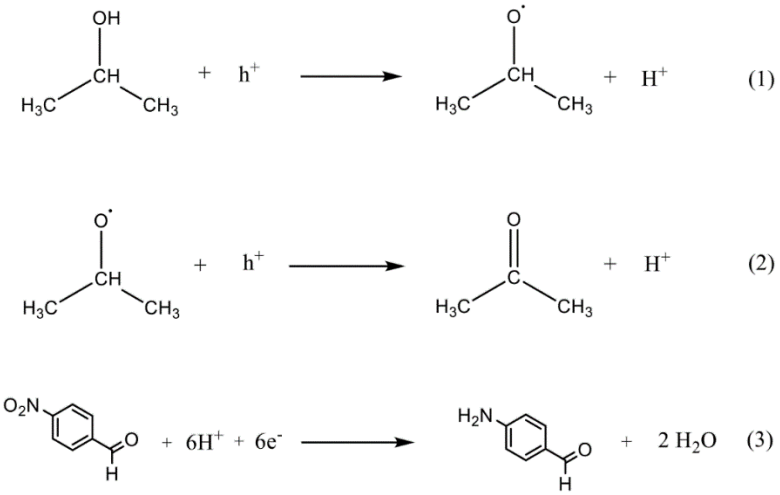

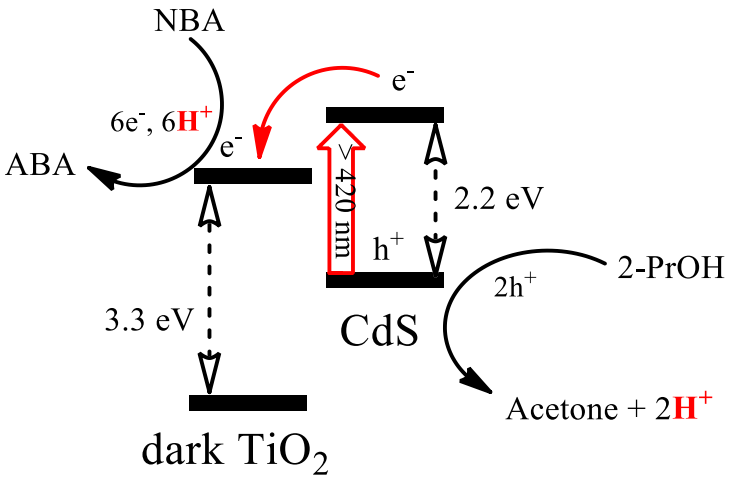

Scheme 1. Proposed photocatalytic mechanism.

2.3. Comparison of the Composites CdS/TiO_2-(1–4)

In Figure 8 the photocatalytic activities of the composite materials are reported for an easy comparison. Among the photocatalysts with a 1:16 ratio (see Table 1) we observe a relation between crystallinity and photocatalytic activity. In fact, the most crystalline CdS/TiO_2-2 and CdS/TiO_2-3 are clearly the most active in the reduction of the nitroaromatic compound. These results could indicate that the increase in TiO_2 crystallinity determines a decrease of surface defects that act as recombination centres. At the same time, considering that the increase of crystallinity is accompanied by an important decrease of surface areas (Table 1), it is clear that high surface area (that could correspond to a larger number of active surface sites) is not required to obtain high photocatalytic activity.

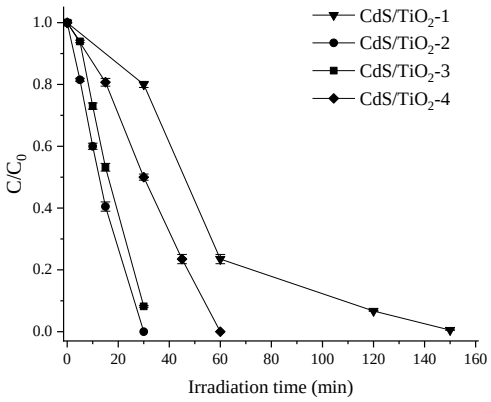

Figure 8. C/C_0 ratio vs. time profiles obtained upon irradiation ($\lambda \geq 420$ nm, 25 °C) of CdS/TiO_2-(1–4) (3 g/L) suspended in a deaerated CH_3CN/2-PrOH (4/1) reaction mixture containing a starting NBA concentration of 1×10^{-4} M.

Otherwise, the combined effect of anatase crystal size decrease and mesoporosity decrease, as observed for the CdS/TiO_2-4 sample, seems to be detrimental for the catalytic activity (Table 1 and Figure S1). In addition, when looking at CdS/TiO_2-4 and CdS/TiO_2-2, the observed decrease in photocatalytic activity of the former is not attributable to a lower amount of CdS because when preparing the materials, we varied the amount of TiO_2 while keeping the amount of CdS, which is the photoactive material, constant. Therefore, the different photocatalytic activity may be related to textural differences in the material rather than optical differences.

From Figure 8, it is seen that C/C_0 vs. time curves do not follow first order kinetics with respect to the NBA concentration. Generally, we can assume that the rate (v) depends on both the concentration of promoted electrons in the acceptor states of CdS and TiO_2 ($[e]^a$) and the concentration of NBA ($[NBA]^b$) according to Equation (4). The low concentration of NBA used for the present study prevents the application of a pseudo-first order approximation. Furthermore, under steady illumination conditions, the concentration of electrons residing in the photocatalyst can be considered constant since the equilibrium between charge generation and recombination is fast compared to the time scales of the photodegradation experiments.

$$-\frac{d([NBA]_0 - [NBA]_t)}{dt} = v = k[e]^a[NBA]_t^b \quad (4)$$

Figure S7 reports the calculated rate values for each CdS/TiO_2-(1–4) and the plot of these rates vs. $[NBA]_t$ shows that v is essentially independent from $[NBA]$, suggesting that $b = 0$. Therefore, the kinetic Equation (4) can be simplified into Equation (5), where the rate is controlled only by the stationary concentration of electrons stored inside the photocatalyst:

$$v = k[e]^a \quad (5)$$

In Table 2 we report the rate values for each CdS/TiO_2-(1–4) calculated after 30 min of irradiation.

Table 2. Rate values (v) after 30 min of irradiation of each CdS/TiO_2 material.

Material	v (10^{-6}) [mol/s]
CdS/TiO_2-2	3.3
CdS/TiO_2-3	3.0
CdS/TiO_2-4	1.7
CdS/TiO_2-1	0.7

The evidence of the photoconversion rate being independent of the concentration of the dye is probably motivated by the fact that the reduction of the azo compound is nearly isoergonic with the occupied electron states in the semiconductor [9,44] and only the highest lying filled electronic states may actually be active in promoting the desired reductive process. We note that the mechanism of this reduction reaction must be complex, since it involves a multielectronic charge transfer possibly accompanied by proton transfer as a charge compensating mechanism. Since, upon illumination, the electronic charge build-up in semiconductor states is charge compensated by protons coming from the concomitant oxidation of the hole scavenger, we found that the kinetics are governed by the reactants (electrons and protons) present at the semiconductor surface rather than by the dye in the solution, indicating that, ostensibly, reductive charge transfer to the azo dye is the kinetically limiting step. The observed order reflects the textural characteristics in terms of crystallinity and mesoporosity needed for obtaining good photocatalytic activity. Moreover, the measured difference of the ns radiative recombination of the carriers on CdS/TiO_2-1 and CdS/TiO_2-2 reported in Section 2.1.2 agrees with the proposed kinetic model of NBA transformation, confirming that in the more crystalline material the charge separation is better achieved, resulting in a higher concentration of photo-promoted electrons active in fostering the conversion of NBA.

2.4. Stability of Composite CdS/TiO_2-2

The results of Section 2.3 demonstrated that the CdS/TiO_2-2 material had the highest photocatalytic activity. In the following, we discuss its recyclability comparing it with that of commercial CdS, which is the benchmark photocatalyst (Figure 9). CdS/TiO_2-2 almost completely transformed NBA to ABA in the first and second cycle, while a decrease of about 10% was observed in the third one. Then the photoactivity remains quite constant in the subsequent runs. As far as commercial CdS is concerned, some important features are observed: (i) commercial CdS always has a lower photocatalytic activity with respect to the composite CdS/TiO_2-2, converting only 47% in the first cycle in 30 min of irradiation, (ii) photostability of commercial CdS is poor since the % of NBA conversion is reduced to less than 10% from the third cycle onward. These data demonstrate that the combination of CdS with another semiconductor, as in the case of CdS/TiO_2-2, provides a new composite material where synergies between the two components allow charge separation and consequent higher photocatalytic activity. Moreover, the problem of low photostability (and low recyclability) of CdS, that usually limits its use as a photocatalyst, can be successfully overcome by CdS/TiO_2-2.

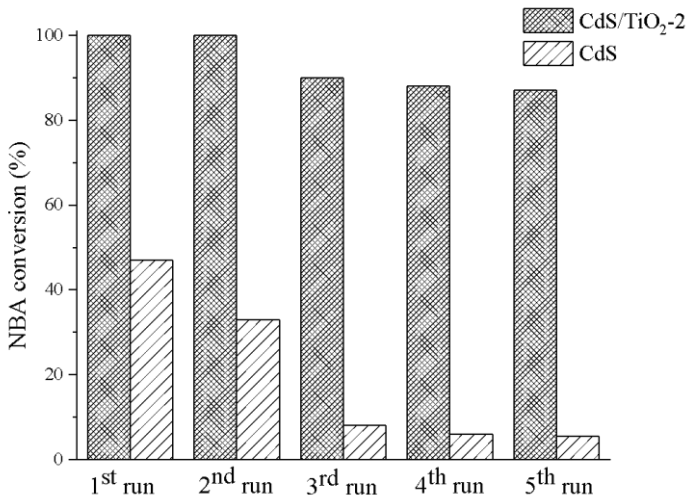

Figure 9. Conversion % of NBA during five repeated experiments obtained upon irradiation ($\lambda \geq 420$ nm, 30 min) of CdS/TiO_2-2 or commercial CdS suspended in a deaerated CH_3CN/2-PrOH (4/1) reaction mixture containing a starting NBA concentration of 1×10^{-4} M.

2.5. Prolonged Irradiation of CdS/TiO_2-2

After prolonged irradiation of the most active CdS/TiO_2-2 sample, we visually observed a darkening of colour. Based on what has already been seen for TiO_2, a possible electron accumulation is hypothesized (with formation of Ti^{3+} centres) preluding the reduction of the aldehyde group to alcohol [28]. The spectral variations recorded after 300′ irradiation (Figure 5) are in agreement with the alcohol formation.

^{1}H-NMR and ESI-MS experiments have also been performed on crude of the reaction irradiated for 300 min. In this case, the absence of peaks in the aldehydes area (8.5–10.5 ppm), in concomitance with the appearance of a peak at 4.55 ppm shows the complete reduction of 4-nitrobenzaldehyde into 4-aminobenzylalcohol (Figure 10). In addition, the presence of a peak at 124.11 m/z is evidence of the amino-alcohol formation:

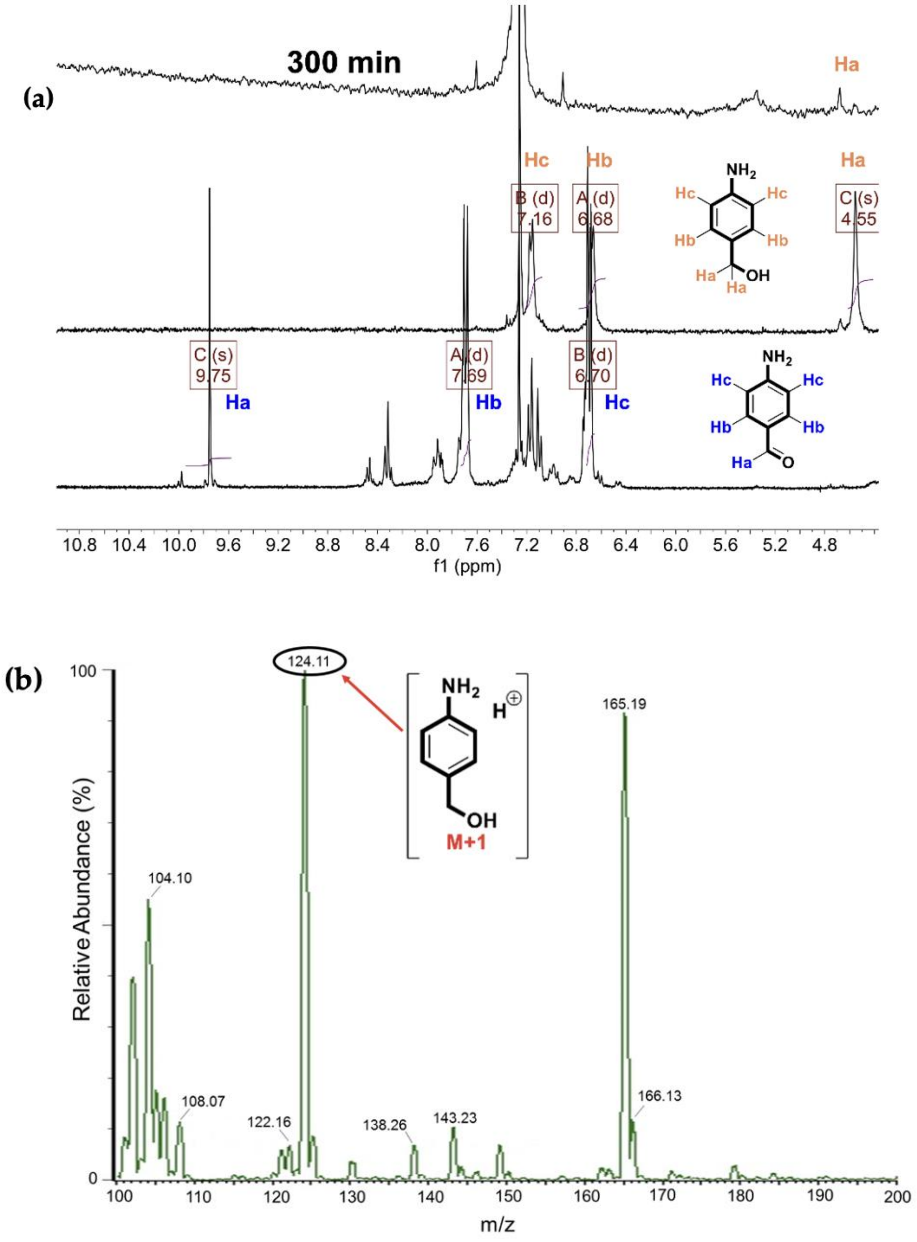

Figure 10. (**a**) from bottom to top the spectra of 4-aminobenzaldehyde, 4-aminobenzyl alcohol and crude of reaction after 300 min of irradiation; (**b**) on right the ESI-MS spectrum of crude of reaction after 300 min.

This result is relevant because the selectivity of the reaction can be controlled when the target molecule has two reducible functional groups.

3. Materials and Methods

3.1. Chemicals

All chemicals and reagents were used without further purifications. Ti (IV) tetra-isopropoxide ($Ti(OiPr)_4$) (97%), Na_2S (98%) and ethylendiaminetetraacetic acid (EDTA) were purchased from Aldrich (St. Louis, MO, USA) and $CdCl_2$ anhydrous (99%) from Alfa Aesar (Karisruhe, Germany). 4-nitrobenzaldehyde (NBA, Fluka AG, Buchs, Switzerland), 4-aminobenzaldehyde (ABA, Fluka, Buchs, Switzerland) and 4-aminobenzylalcohol (Fluka, Buchs, Switzerland) were used as target and authentic products in ^1H NMR experiments, respectively. Acetonitrile (CH_3CN, BDH Chemicals, Dubai, UAE), 2-PrOH (C_3H_8O, Fluka, Buchs, Switzerland), EtOH (C_2H_6O, Fluka, Buchs, Switzerland) were used as solvents without any purification.

3.2. Preparation of Colloidal CdS Nanoparticles

A stable aqueous colloidal solution of nanoparticles of cadmium sulfide was obtained by the method of chemical condensation [45]. In brief, water solutions of $CdCl_2$ (12.5 mM), Na_2S (12.5 mM), and EDTA (12.5 mM) were prepared and then mixed in equal volumes (10 mL) by shaking at room temperature for some minutes. Prior to mixing, the pH of the EDTA water solution was adjusted at around 5: at this pH, EDTA molecules dissociated and behaved as anions. As a result, they became capping ligands for Cd^{2+}. When the overall solution was subjected to shaking, the EDTA-anions formed amphiphilic, negatively charged shells that made CdS Quantum Dots (QDs) water-soluble. The solution obtained had a yellow colour. Stable colloidal CdS QDs played the role of crystal seeds for nucleation and formation of anatase TiO_2 and remained well dispersed.

3.3. Preparation of Colloidal CdS/TiO_2 Composites

In situ doping of amorphous TiO_2 by CdS QDs was carried out following a reported direct hydrolysis route [40]. Specifically, a measured amount of $Ti(OiPr)_4$ (0.6 mL–2 mmol) was slowly added to the aqueous colloidal solution of CdS (10 mL, 0.125 mmol) that acts as the hydrolysing agent. The solution was heated up to 90 °C under continuous stirring and aged at this temperature for different periods (0′, 60′, 180′). Later on, the water evaporated, and the recovered yellowish powder was rinsed with ethanol and water and then dried in oven overnight (40 °C) under aerated conditions. The obtained samples are called CdS/TiO_2-1, CdS/TiO_2-2 and CdS/TiO_2-3, respectively. In addition, another photocatalyst was prepared by hydrolyzing $Ti(OiPr)_4$ (0.3 mL–1 mmol) in an aqueous colloidal solution of CdS (10 mL, 0.125 mmol) followed by an aging period of 60′. This last powder was indicated as CdS/TiO_2-4. From each preparation, about 0.5 g of solid CdS/TiO_2 was obtained.

3.4. X-ray Diffraction

Material crystalline structures were analysed by means of Malvern Panalytical X'Pert diffractometer (Malvern, UK), using Cu Kα as a source of radiation (λ = 1.541874 Å) and the diffractograms elaborated by X'Pert Highscore software (JCPDS files).

The crystalline domain sizes were calculated by means of the Debye–Scherrer equation using the following online calculator: XRD Crystallite (grain) Size Calculator (Scherrer Equation)—InstaNANO. https://instanano.com/characterization/calculator/xrd/crystallite-size/.

3.5. (High-Resolution) Transmission Electron Microscopy

The Energy-Dispersive X-rays Spectroscopy (EDS) measurements were performed with AZtecLive & ULTIM Max EDS System: DETECTOR OXFORD EDS Ultim Max—Software AZTEC.

3.6. Specific Surface Area and Porosity Measurements

ASAP2020 by Micromeritics (Norcross, GA, USA) was used as a gas-volumetric instrument for the determination of nitrogen adsorption/desorption isotherms at the temperature of −196 °C. The BET model and DFT method (slit pores) were applied to evaluate the exposed surface area and porosity of the materials. Prior to nitrogen adsorption, all the powders were outgassed overnight at the temperature of 80 °C (residual pressure 10^{-2} mbar) in order to remove atmosphere molecules adsorbed onto the surface and into the pores.

3.7. Single Photon Counting

Emission lifetimes of CdS/TiO_2-1, CdS/TiO_2-2 and CdS powders were acquired with a Picoquant Picoharp 300 time correlated single photon counting at a 4 ps resolution using a 460 nm pulsed LED source. Levenberg–Marquardt fitting/deconvolution of the decay histogram was accomplished with a tri- and bi-exponential function by the dedicated Fluofit program. In general, fits satisfied the statistical acceptability criteria, with $\chi \cong 1$ and residuals R(i) = W(i)(Decay(i) − Fit(i)) < 4 standard deviations fluctuating around 0 within all the fitting intervals.

3.8. DR UV-vis Measurements

Absorption spectra of CdS/TiO_2-(1–4) powders were collected under diffuse reflectance (R%) mode with a JASCO V 570 (Tokyo, Japan) spectrophotometer equipped with an integrating sphere.

3.9. Infrared Measurements

Infrared spectra were recorded with a Nicolet 510P (Waltham, MA, USA) FTIR instrument in KBr, fitted with a Spectra-Tech collector diffuse reflectance accessory (range 4000 to 200 cm^{-1}). The samples were prepared using an aliquot (10 mg) of the chosen CdS/TiO_2 material, which was put in contact with a CH_3CN/2-PrOH (4/1) solution of NBA (1×10^{-4} M). The suspensions were stirred at room temperature until the evaporation of the solvent was complete. Then the powder impregnated with the nitrocompound was dried overnight in the oven. In the case of the irradiated experiments, then chosen CdS/TiO_2 (10 mg) was suspended in CH_3CN/2-PrOH (4/1, 3 mL) containing NBA (1×10^{-4} M), then the suspension was degassed and irradiated ($\lambda \geq 420$ nm). After irradiation, the solvent was evaporated, and the powder was dried overnight. An analogous sample was obtained without irradiation. For the sake of comparison, pure NBA was also examined.

3.10. Photocatalytic Experiments

Typically, each CdS/TiO_2-(1–4) (3 g/L) powder was suspended in a CH_3CN/2-PrOH (4/1, 3 mL) mixture containing 4-nitrobenzaldehyde (1×10^{-4} M, NBA) inside a spectrophotometric cell. The cell was closed and degassed by N_2 bubbling for 20 min, then the suspension was placed in front of the lamp (HeliosItalquartz, Hg medium pressure) and illuminated for the desired period using a cut off filter ($\lambda \geq 420$ nm). After the irradiation, the suspension was centrifuged, and the evolution of the reaction was monitored by UV-visible spectrophotometry in the 200–600 nm interval (Cary 300 UV-vis double beam spectrophotometer Agilent Technologies). Concentration of NBA and of 4-aminobenzaldehyde (ABA) vs. time profiles were built after the determination of ε_{264} and of ε_{312} values (14,670 M^{-1} cm^{-1} and 20,300 M^{-1} cm^{-1}, respectively) from calibration curves by using authentic samples. When requested, KBr was added after irradiation to facilitate the deposition of the photocatalyst powder and its separation from the solution. Catalyst stability was evaluated by employing the same photocatalyst for repeated runs. Between repetitions, the irradiated powder was rinsed with the same solvent used in the photocatalytic experiment and dried in air at room temperature. Catalyst stability was evaluated by employing CdS/TiO_2-2 and CdS in three consecutive irradiation experiments (30 min each). Between two subsequent cycles, the recovered powders were rinsed CH_3CN and dried in air at room temperature.

3.11. ESI MS Spectra

Mass spectral analyses of the photocatalytic reaction mixture were performed using an ESI MICROMASS ZMD 2000 (Markham, ON, Canada) electrospray mass spectrometer. Samples were prepared by dissolving 200 µL of reaction crude in 1 mL solution composed by 1% of TFA (*v*/*v*) in CH_3CN. ESI MS operated in positive ionization mode.

3.12. NMR Measurements

^1H NMR spectra were recorded in $CDCl_3$ solution using 5 mm tubes, at 296 K with a Varian Gemini 300 (Palo Alto, CA, USA), operating at 400 MHz (^1H) and using standard pulse sequences from the Varian library. The chemical shifts were referenced to the $CDCl_3$ signal: δ (H) 7.26 ppm. The relaxation delay between the successive pulse cycle was 1.0 s.

4. Conclusions

Composite CdS/TiO_2 powders were successfully prepared by hydrolysis of a titanium alkoxide on colloidal CdS. Textural characterization (XRD, HRTEM, FESEM, EDS) evidenced the presence of anatase crystalline domains (of nanometric size), and of homogeneously dispersed CdS particles (acting as seeds for anatase growing). The intimate contact between CdS and TiO_2 is confirmed by single photon time emission decays analysis with the longer lifetimes of separated charges in the larger crystalline materials.

A correlation among textural characteristics and photocatalytic properties pointed out that the nanometric size of anatase crystalline domains, the presence of dispersed CdS, and the presence of mesopores as nanoreactors, where the intimate interaction surface/reactant occurs, are necessary for obtaining noticeable photoreactivity in the reductive transformation of 4-nitrobenzaldehyde to the corresponding aniline.

We believe that this work sheds light on the textural parameters important for the development of photocatalytically effective materials. In addition, the combination of TiO_2 with CdS increases the photostability of the photoactive material, thus opening up the possibility of photocatalytic transformations under visible light conditions.

Supplementary Materials: The following supporting information can be downloaded at: https://www.mdpi.com/article/10.3390/catal13010074/s1, Figure S1: (A) Adsorption/desorption isotherms of CdS/TiO_2 samples; (B) Pore size distribution curves. The broken line indicates the threshold between micro and meso/macropores; (C) Pore area distribution curves. The logarithmic scale, where used, allows better evidencing of the large pore region. The broken lines indicate the threshold between micro and meso/macropores. Figure S2: Single photon time emission decay of powder CdS/TiO_2-1. Figure S3: Single photon time emission decay of powder CdS/TiO_2-2. Figure S4: Energy band gap of CdS/TiO_2-(1–4) obtained using the baseline method (Ref. [33]) coupled with that described by Tauc: for TiO_2 the fundamental fit is applied using the relation $(Fh\nu)\alpha = A \times (h\nu - Eg)$, where F is the Kubelka–Munk coefficient, $\alpha = 1/2$ for an indirect band gap, A is a proportionality constant and hν is the photon energy; additionally, a linear fit used as an abscissa is applied for the slope below the fundamental absorption. An intersection of the two fitting lines gives the band energy estimation (red); Figure S5: Spectral changes obtained upon visible irradiation of deaerated suspensions of CdS/TiO_2-2 (3 g/L) in CH_3CN/2-PrOH (4/1, 3 mL) mixture containing NBA (1×10^{-4} M); Figure S6: Decrease of NBA concentration as a function of irradiation time for CdS/TiO_2-2 (squares), CdS (circles) and TiO_2 (triangles). The experimental conditions are the same as Figure 5. Values of CdS/TiO2-2 (already present in Figure 5) are reported here for an easy comparison. Figure S7: Decrease of NBA concentration obtained by irradiating (λ > 420 nm, 30 min) CdS/TiO_2-2 or CdS during three consecutive experiments. Figure S8: Spectral changes obtained upon prolonged visible irradiation (300 min) of a deaerated suspension of CdS/TiO_2-2 (3 g/L) in CH_3CN/2-PrOH (4/1, 3 mL) mixture containing NBA (1×10^{-4} M); Table S1: Band gap values obtained from Figure S4.

Author Contributions: Data curation, M.M. (Martina Milani), M.M. (Michele Mazzanti), G.M., G.D.C. and A.M.; investigation, M.M. (Martina Milani), M.M. (Michele Mazzanti), G.M., G.D.C. and S.C.; methodology, M.M. (Martina Milani), M.M. (Michele Mazzanti), G.M. and G.D.C.; supervision, A.M. and G.M.; writing—original draft, A.M. and G.M.; writing—review & editing, A.M. All authors have read and agreed to the published version of the manuscript.

Funding: The research was funded by University of Ferrara, (FAR 2020, FAR 2021) with the contribution of the EU H2020 Research Innovation Actions 2020–2024 "CONDOR" (grant agreement No 101006839).

Data Availability Statement: The data used to support the findings of this study are included within the article.

Acknowledgments: We kindly acknowledge Lorenza Marvelli for her help in the FT-IR measurements and Maria Carmen Valsania for electron microscopy measurements.

Conflicts of Interest: The authors declare no conflict of interest.

References

1. Palmisano, G.; Augugliaro, V.; Pagliaro, M.; Palmisano, L. Photocatalysis: A promising route for 21st century organic chemistry. *Chem. Commun.* **2007**, *33*, 3425–3437. [CrossRef] [PubMed]
2. Verma, R.; Gangwar, J.; Srivastava, A.K. Multiphase TiO_2 nanostructures: A review of efficient synthesis, growth mechanism, probing capabilities, and applications in bio-safety and health. *RSC Adv.* **2017**, *7*, 44199–44224. [CrossRef]
3. Ge, M.; Cao, C.; Huang, J.; Li, S.; Chen, Z.; Zhang, K.-Q.; Al-Deyab, S.S.; Lai, Y. A review of one-dimensional TiO_2 nanostructured materials for environmental and energy applications. *J. Mater. Chem. A* **2016**, *4*, 6772–6801. [CrossRef]
4. Liu, J.; Meeprasert, J.; Namuangruk, S.; Zha, K.; Li, H.; Huang, L.; Shi, L.-Y.; Zhang, D. Facet-activity relationship of TiO_2 in Fe_2O_3/TiO_2 nanocatalysts for selective catalytic reduction of NO with NH_3: In situ DRIFTs and DFT studies. *J. Phys. Chem. C* **2017**, *121*, 4970–4979. [CrossRef]
5. Li, G.; Huang, J.; Chen, J.; Deng, Z.; Huang, Q.; Liu, Z.; Guo, W.; Cao, R. Highly active photocatalyst of Cu_2O/TiO_2 octahedron for hydrogen generation. *ACS Omega* **2019**, *4*, 3392–3397. [CrossRef] [PubMed]
6. Luo, X.; Deng, F.; Min, L.; Luo, S.; Guo, B.; Zeng, G.; Au, C. Facile one-step synthesis of inorganic-framework molecularly imprinted TiO_2/WO_3 nano-composite and its molecular recognitive photocatalytic degradation of target contaminant. *Environ. Sci. Technol.* **2013**, *47*, 7404–7412. [CrossRef] [PubMed]
7. David, S.; Mahadik, M.A.; Chung, H.S.; Ryu, J.H.; Jang, J.S. Facile hydrothermally synthesized a novel CdS nanoflower/rutile TiO_2 nanorod heterojunction photoanode used for photoelectrocatalytic hydrogen generation. *ACS Sustain. Chem. Eng.* **2017**, *5*, 7537–7548. [CrossRef]
8. Gao, X.; Liu, X.; Zhu, Z.; Gao, Y.; Wang, Q.; Zhu, F.; Xie, Z. Enhanced visible light photocatalytic performance of CdS sensitized TiO_2 nanorod arrays decorated with Au nanoparticles as electron sinks. *Sci. Rep.* **2017**, *7*, 973–982. [CrossRef]
9. Mazzanti, M.; Milani, M.; Cristino, V.; Boaretto, R.; Molinari, A.; Caramori, S. Visible light reductive photocatalysis of azo-dyes with n–n junctions based on chemically deposited CdS. *Molecules* **2022**, *27*, 2924–2939. [CrossRef]
10. Xie, Z.; Liu, X.; Wang, W.; Wang, X.; Liu, C.; Xie, Q.; Li, Z.; Zhang, Z. Enhanced photoelectrochemical and photocatalytic performance of TiO_2 nanorod arrays/CdS quantum dots by coating TiO_2 through atomic layer deposition. *Nano Energy* **2015**, *11*, 400–408. [CrossRef]
11. Xue, Y.; Wu, Z.; He, X.; Yang, X.; Chen, X.; Gao, Z. Constructing a Z- scheme heterojunction of egg-like core@shell CdS@TiO_2 photocatalyst via a facile reflux method for enhanced photocatalytic performance. *Nanomaterials* **2019**, *9*, 222. [CrossRef] [PubMed]
12. Janbandhu, S.Y.; Joshi, A.; Munishwar, S.R.; Gedam, R.S. CdS/TiO_2 heterojunction in glass matrix: Synthesis, characterization, and application as an improved photocatalyst. *Appl. Surf. Sci.* **2019**, *497*, 143758. [CrossRef]
13. Shah, L.A.; Haleem, A.; Sayed, M.; Siddiq, M. Synthesis of sensitive hybrid polymer microgels for catalytic reduction of organic pollutants. *J. Environ. Chem. Eng.* **2016**, *4*, 3492–3497. [CrossRef]
14. Low, J.; Dai, B.; Tong, T.; Jiang, C.; Yu, J. In situ irradiated X-ray photoelectron spectroscopy investigation on a direct Z-scheme TiO_2/CdS composite film photocatalyst. *Adv. Mater.* **2019**, *31*, 1802981. [CrossRef] [PubMed]
15. Zhou, P.; Le, Z.; Xie, Y.; Fang, J.; Xu, J. Studies on facile synthesis and properties of mesoporous CdS/TiO_2 composite for photocatalysis applications. *J. Alloys Compd.* **2017**, *692*, 170–177. [CrossRef]
16. Ge, H.; Xu, F.; Cheng, B.; Yu, J.; Ho, W. S-scheme heterojunction TiO_2/CdS nanocomposite nanofiber as H_2-production photocatalyst. *ChemCatChem* **2019**, *11*, 6301–6309. [CrossRef]
17. Liu, S.; Zhang, N.; Tang, Z.R.; Xu, Y.J. Synthesis of onedimensional CdS@TiO_2 core−shell nanocomposites photocatalyst for selective redox: The dual role of TiO_2 shell. *ACS Appl. Mater. Interfaces* **2012**, *4*, 6378–6385. [CrossRef]
18. Li, H.; Eastman, M.; Schaller, R.; Hudson, W.; Jiao, J. Hydrothermal synthesis of CdS nanoparticle-decorated TiO_2 nanobelts for solar cell. *J. Nanosci. Nanotechnol.* **2011**, *11*, 8517–8521. [CrossRef]
19. Bessekhouad, Y.; Robert, D.; Weber, J.V. Bi_2S_3/TiO_2 and CdS/TiO_2 heterojunctions as an available configuration for photocatalytic degradation of organic pollutant. *J. Photochem. Photobiol. A Chem.* **2004**, *163*, 569–580. [CrossRef]
20. Hamdi, A.; Ferreira, D.P.; Ferraria, A.M.; Conceição, D.S.; Vieira Ferreira, L.F.; Carapeto, A.P.; Boufi, S.; Bouattour, S.; Botelho do Rego, A.M. TiO_2-CdS nanocomposites: Effect of CdS oxidation on the photocatalytic activity. *J. Nanomater.* **2016**, *2016*, 6581691. [CrossRef]
21. Du, Y.-E.; Niu, X.; He, X.; Hou, K.; Liu, H.; Zhang, C. Synthesis and photocatalytic activity of TiO_2/CdS nanocomposites with co-exposed anatase highly reactive facets. *Molecules* **2021**, *26*, 6031–6047. [CrossRef] [PubMed]

22. Mahmood, A.; Park, J.-W. TiO_2/CdS nanocomposite stabilized on a magnetic-cored dendrimer for enhanced photocatalytic activity and reusability. *J. Colloid Interface Sci.* **2019**, *555*, 801–809. [CrossRef] [PubMed]
23. Peng, S.; Huang, Y.; Li, Y. Rare earth doped TiO_2-CdS and TiO_2-CdS composites with improvement of photocatalytic hydrogen evolution under visible light irradiation. *Mater. Sci. Semicond. Process.* **2013**, *16*, 62–69. [CrossRef]
24. Wu, K.; Wu, P.; Zhu, J.; Liu, C.; Dong, X.; Wu, J.; Meng, G.; Xu, K.; Hou, J.; Liu, Z.; et al. Synthesis of hollow core-shell CdS@TiO_2/Ni_2P photocatalyst for enhancing hydrogen evolution and degradation of MB. *Chem. Eng. J.* **2019**, *360*, 221–230.
25. Xie, J.; Hong, W.; Meng, M.; Tian, M.; Kang, C.; Zhou, Z.; Chen, C.; Tang, Y.; Luo, G. Synthesis and photocatalytic activity of cerium-modified CdS-TiO_2 photocatalyst for the formaldehyde degradation at room temperature. *Z. Anorg. Allg. Chem.* **2018**, *644*, 1570–1575.
26. Hu, Z.; Quan, H.; Chen, Z.; Shao, Y.; Li, D. New insight into an efficient visible light-driven photocatalytic organic transformation over CdS/TiO_2 photocatalysts. *Photochem. Photobiol. Sci.* **2018**, *17*, 51–59. [CrossRef] [PubMed]
27. Tafesh, A.M.; Weiguny, J. A review of the selective catalytic reduction of aromatic nitro compounds into aromatic amines, isocyanates, carbamates, and ureas using CO. *Chem. Rev.* **1996**, *96*, 2035–2052. [CrossRef]
28. Molinari, A.; Maldotti, A.; Amadelli, R. Probing the role of surface energetics of electrons and their accumulation in photoreduction processes on TiO_2. *Chem. Eur. J.* **2014**, *20*, 7759–7765. [CrossRef]
29. Molinari, A.; Mazzanti, M.; Fogagnolo, M. Photocatalytic selective reduction by TiO_2 of 5-nitrosalicylic acid ethyl ester: A mild route to mesalazine. *Catal. Lett.* **2020**, *150*, 1072–1080. [CrossRef]
30. Ferry, J.L.; Glaze, W.H. Photocatalytic reduction of nitro organics over illuminated titanium dioxide: Role of the TiO_2 surface. *Langmuir* **1998**, *14*, 3551–3555. [CrossRef]
31. Imamura, K.; Iwasaki, S.; Maeda, T.; Hashimoto, K.; Ohtani, B.; Kominami, H. Photocatalytic reduction of nitrobenzenes to aminobenzenes in aqueous suspensions of titanium(iv)oxide in the presence of hole scavengers under deaerated and aerated conditions. *Phys. Chem. Chem. Phys.* **2011**, *13*, 5114–5119. [CrossRef] [PubMed]
32. Shiraishi, Y.; Hirakawa, H.; Togawa, Y.; Sugano, Y.; Ichikawa, S.; Hirai, T. Rutile crystallites isolated from degussa (evonik) P25 TiO_2: Highly efficient photocatalyst for chemoselective hydrogenation of nitroaromatics. *ACS Catal.* **2013**, *3*, 2318–2326. [CrossRef]
33. Kaur, J.; Pal, B. 100% selective yield of m-nitroaniline by rutile TiO_2 and m-phenylenediamine by P25-TiO_2 during m-dinitrobenzene photoreduction. *Catal. Commun.* **2014**, *53*, 25–28. [CrossRef]
34. Wang, H.; Yan, J.; Chang, W.; Zhang, Z. Practical synthesis of aromatic amines by photocatalytic reduction of aromatic nitro compounds on nanoparticles N-doped TiO_2. *Catal. Commun.* **2009**, *10*, 989–994. [CrossRef]
35. Lu, C.; Yin, Z.; Sun, C.; Chen, C.F.; Wang, F. Photocatalytic reduction of nitroaromatics into anilines using CeO_2-TiO_2 nanocomposite. *Mol. Catal.* **2021**, *513*, 111775–111782. [CrossRef]
36. Kaur, R.; Pal, B. Cu nanostructures of various shapes and sizes as superior catalysts for nitro-aromatic reduction and co-catalyst for Cu/TiO_2 photocatalysis. *Appl. Catal. A Gen.* **2015**, *491*, 28–36. [CrossRef]
37. Zelekew, O.A.; Kuo, D. Facile synthesis of SiO_2@CuxO@TiO_2 heterostructures for catalytic reductions of 4-nitrophenol and 2-nitroaniline organic pollutants. *Appl. Surf. Sci.* **2017**, *393*, 110–118. [CrossRef]
38. Molinari, A.; Maldotti, A.; Amadelli, R. Effect of the electrolyte cations on photoinduced charge transfer at TiO_2. *Catal. Today* **2017**, *281*, 71–77. [CrossRef]
39. Ibrahim, M.A.M.; Van-Duong, D.; Ahmed, S.Y.; Nasser, A.M.B.; Ho-Suk, C. Design of an efficient photoanode for dye-sensitized solar cells using electrospun one-dimensional GO/N-doped nanocomposite SnO_2/TiO_2. *Appl. Surf. Sci.* **2017**, *400*, 355–364.
40. Vorokh, A.S.; Kozhevnikova, N.S.; Gorbunova, T.I.; Gyrdasova, O.I.; Baklanova, I.V.; Buldakova, L.Y.; Yanchenko, M.Y.; Murzakaev, A.M.; Shalaeva, E.V.; Enyashin, A.N. Facile, rapid and efficient doping of amorphous TiO_2 by presynthesized colloidal CdS quantum dots. *J. Alloys Compd.* **2017**, *706*, 205–214. [CrossRef]
41. Yan, J.; Wu, G.; Guan, N.; Li, L.; Li, Z.; Cao, X. Understanding the effect of surface/bulk defects on the photocatalytic activity of TiO_2: Anatase versus rutile. *Phys. Chem. Chem. Phys.* **2013**, *15*, 10978–10988. [CrossRef] [PubMed]
42. Marschall, R. Semiconductor composites: Strategies for enhancing charge carrier separation to improve photocatalytic activity. *Adv. Funct. Mater.* **2014**, *24*, 2421–2440. [CrossRef]
43. Makula, P.; Pacia, M.; Macyk, W. How to correctly determine the band gap energy of modified semiconductor photocatalysts based on UV-Vis spectra. *J. Phys. Chem. Lett.* **2018**, *9*, 6814–6817. [CrossRef] [PubMed]
44. Mazzanti, M.; Caramori, S.; Fogagnolo, M.; Cristino, V.; Molinari, A. Turning waste into useful products by photocatalysis with nanocrystalline TiO_2 thin films: Reductive cleavage of azo bond in the presence of aqueous formate. *Nanomaterials* **2020**, *10*, 2147–2164. [CrossRef] [PubMed]
45. Kozhevnikova, N.S.; Vorokh, A.S.; Rempel, A.A. Preparation of stable colloidal solution of cadmium sulfide cds using ethylenediaminetetraacetic acid. *Russ. J. Gen. Chem.* **2010**, *80*, 391–394. [CrossRef]